Applied Catalysis A, General 556 (2018) 64–72

Contents lists available at ScienceDirect

Applied Catalysis A, General

journal homepage: www.elsevier.com/locate/apcata

Dependence of H_2 and CO_2 selectivity on Cu oxidation state during partial oxidation of methanol on Cu/ZnO

Hao Chi[a], Christopher M. Andolina[a], Jonathan Li[b], Matthew T. Curnan[a], Wissam A. Saidi[c], Guangwen Zhou[b], Judith C. Yang[a,c], Götz Veser[a,d,*]

[a] Department of Chemical and Petroleum Engineering, University of Pittsburgh, Pittsburgh, PA, 15216, USA
[b] Department of Mechanical Engineering, State University of New York, Binghamton, NY, 13902, USA
[c] Department of Materials Science and Engineering, University of Pittsburgh, Pittsburgh, PA, 15261, USA
[d] Center for Energy, University of Pittsburgh, PA, 15261, USA

ARTICLE INFO

Keywords:
Methanol partial oxidation
Cu/ZnO catalyst
H_2 pRoduction
Reaction mechanism
X-ray photoelectron spectroscopy

ABSTRACT

Partial oxidation of methanol is a promising reaction for on-board production of high purity H_2 streams for fuel cell applications. In the present work, the influence of Cu oxidation state on the selectivity of POM catalyzed by Cu/ZnO was investigated via the use of a microreactor and X-ray photoelectron spectroscopy. A strong correlation between H_2 selectivity and the metallic copper (Cu°) content of the catalyst was observed, while, surprisingly, the CO_2 selectivity was not significantly affected by the catalyst oxidation state. Instead, CO_2 selectivity showed a strong correlation with O_2 partial pressure, which could be explained by differences in the energy barriers between CO desorption and CO_2 formation from CO* on Cu_2O surfaces calculated via first-principles calculations. Our results indicate that maintaining metallic Cu catalyst during methanol oxidation could maximize H_2 production for use in fuel cells or other clean energy applications.

1. Introduction

Pollution problems caused by the combustion of fossil fuels necessitate the search for cleaner and more sustainable fuels. Methanol is a promising candidate as a clean fuel due to its high energy density, easy storage, and transportation. Methanol can be used in direct methanol fuel cells to generate electricity or H_2 fuel cells to power mobile devices [1–3]. For use in H_2 fuel cells, a H_2-rich gas mixture can be obtained exothermically at relatively low temperatures (200–300 °C) through the partial oxidation of methanol (POM) [Eq. (1)] [4–7].

$$CH_3OH + 0.5O_2 \rightarrow CO_2 + 2H_2 \quad \Delta H^{\circ} = -192.2 kJ/mol \tag{1}$$

However, incomplete understanding of the POM reaction mechanism and catalyst design still hamper the practical utilization of POM. Cu-based catalysts have been used in methanol synthesis and methanol oxidation for decades [4,8]. Despite long-standing efforts towards developing Cu-based catalysts to address clean energy needs, we are still far from a rational design of Cu-based catalysts in terms of nanoscale structures, metal-support interfaces, as well as chemical states of the catalysts. Much effort has been invested in understanding the impact of Cu loading and the addition of metal promoters, in order to improve catalyst stability and catalytic performance [4,5,9–12]. However, the Cu active phase is still debated. Both Cu° and Cu^{1+} species have been speculated to be essential for hydrogen generation from methanol [6,13]. Moreover, other studies have suggested that, under similar conditions, Cu° is active for methanol oxidation to H_2 and CO_2, Cu^{1+} is active for H_2O and CO formation, and Cu^{2+} – as the least active species – only produces H_2O and CO_2 [5,10,14]. Recent work furthermore has shown that co-feeding product gas (H_2 and CO_2) to the reaction can modify the oxidation state of Cu and hence its catalytic performance. This work suggested that higher Cu° and Cu^{1+} content leads to higher H_2 selectivity [14]. However, mechanistic insight into the correlation between Cu oxidation state and POM reaction selectivity is still largely lacking.

In the present work, 30 wt% Cu/ZnO catalysts were synthesized and evaluated in POM. Methanol conversion, and H_2 and CO_2 selectivity were monitored as a function of the oxidation state of the active Cu phase in the catalyst, in order to elucidate correlations between these experimental observables with different O_2 feed conditions. X-ray photoelectron spectroscopy (XPS) was used to characterize the Cu oxidation states of the catalyst at various stages of the reaction. Based on the experimental observations, POM reaction pathways on Cu_2O and Cu surfaces are proposed, and key assumptions are probed using density functional theory (DFT) calculations in order to gain an improved

* Corresponding author at: Department of Chemical and Petroleum Engineering, University of Pittsburgh, Pittsburgh, PA, 15216, USA.
E-mail address: hac82@pitt.edu (H. Chi).

https://doi.org/10.1016/j.apcata.2018.02.028
Received 18 December 2017; Received in revised form 9 February 2018; Accepted 23 February 2018
Available online 24 February 2018
0926-860X/

atomistic understanding of the POM mechanism as a function of reaction conditions.

2. Experimental methods

2.1. Catalyst preparation

30 wt% Cu/ZnO nanoparticle (NP) catalysts were prepared by co-precipitation from an aqueous zinc and copper nitrate solution. Specifically, $Cu(NO_3)_2{\cdot}3H_2O$ and $Zn(NO_3)_2{\cdot}6H_2O$ (both > 99%, Sigma-Aldrich) were dissolved in deionized water (Milli-Q, 18.2 MΩ cm) to make a 1 M metal nitrate solution with a mass ratio of Cu:Zn = 3:7·Na_2CO_3 (> 99%, Sigma-Aldrich) was dissolved in deionized water to make 1 M solution as a precipitation agent. The mixed metal solution (50 ml) was added dropwise to 300 mL of deionized water at 70 °C under stirring. The pH was monitored by pH meter (OAKTON) and maintained at pH = 7 by adding Na_2CO_3 solution via a burette. The mixture was stirred at 70 °C for 2 h; during this time, the pH increased to ~8.4. The resulting blue precipitate was then separated by centrifugation and washed with deionized water until the pH was 7. The remaining paste was dried at around 90 °C in a vacuum oven overnight and calcined in air at 400 °C for 3 h.

2.2. Catalyst characterization

X-ray diffraction (XRD; Bruker D8) was used to check the catalyst crystal phase, using CuK_α radiation at a wavelength of 1.54 Å, a beam voltage of 40 kV, and a current of 40 mA. The pattern was recorded with a 2θ range from 20° to 90° and a scanning rate of 3.5° min^{-1}. After baseline subtraction and smoothing via fast Fourier transform (FFT), the particle sizes of Cu, CuO, and ZnO were calculated using the Scherrer formula.

Scanning electron microscopy (SEM, JEOL JSM-6510LV) was used to determine the catalyst morphology at low magnification (X3300) with a beam voltage of 15 kV. In order to increase the electron conductivity of the sample and avoid charging effects, a thin palladium film was sputter-coated onto the sample surface before measurement. The elemental composition was determined by using an energy dispersive X-ray spectroscopy (EDX) detector mounted on the SEM device.

High-resolution transmission electron microscopy (HRTEM, JEOL JEM-2100F) was used to observe catalyst morphology at the nanoscale with an accelerating voltage of 200 kV. The TEM sample was prepared by re-dispersing powder in an ethanol solution, dropping solution on a Cu type-B support grid (Ted Pella, Inc.) and vacuum drying. The size distributions of the resulting NPs were determined using TEM images from various areas on the grid. ImageJ 1.47d (National Institutes of Health, USA) was used to measure NP sizes and generate a histogram. In order to generate an elemental mapping from the high-resolution image, different crystal phases were identified from FFT processed images of lattice fringes of the crystals (Fig. S1A). By applying masks on a given lattice position in an FFT processed image and inverting those positions, spatial locations of Cu and ZnO were obtained and colored in red and blue, respectively.

2.3. Reactivity measurements

The conversion of methanol (> 99.8%, Fisher Scientific), as well as H_2 and CO_2 selectivities, were determined in an in-house manufactured microreactor made of an iron/chromium alloy coated with Au to avoid blind activity (as verified over the range of experimental conditions). The 30 wt% Cu/ZnO catalyst (2 mg) was packed inside the microreactor and methanol was introduced to the setup through a syringe pump at an injection rate of 0.127 cc/h. The entire setup was maintained at 200 °C via heating tape in order to avoid condensation of reactants or products. The molar ratio between O_2 (99.995%, Matheson) and methanol was controlled at 0.1, 0.3, and 0.5. Ar (99.995%, Matheson) was used as a carrier gas to maintain a fixed gas hourly space velocity (GHSV) of 3150 h^{-1}. Methanol molar concentration in the feed gas (MeOH, O_2, and Ar) was fixed at 62.5 mol%. The outlet gas composition which consisted of only H_2, H_2O, CO_2, CO and methanol was measured by a mass spectrometer (Pfeiffer Omnistar QMS 200), and the corresponding molar flow rates (ni) were calculated.

The experiments were run until steady state was attained (defined as no more than 10% change of measured concentrations over 10 min) which occurred within 1 h for all experiments shown. The selectivity (S) and conversion (X) of various gaseous products were calculated according to Eqs. (2)–(4):

$$X_{CH_3OH} = \frac{n_{CH_3OH,in} - n_{CH_3OH,out}}{n_{CH_3OH,in}} \times 100\% \quad (2)$$

$$S_{H_2} = \frac{n_{H_2}}{2 \times (n_{CH_3OH,in} - n_{CH_3OH,out})} \times 100\% \quad (3)$$

$$S_{CO_2} = \frac{n_{CO_2}}{n_{CH_3OH,in} - n_{CH_3OH,out}} \times 100\% \quad (4)$$

Since CO, CO_2, H_2, and H_2O were the only detectable products, CO and H_2O selectivities are simply the "mirror image" of CO_2 and H_2 selectivities (i.e. $S_{CO2} = 1 - S_{CO2}$ and $S_{H2O} = 1 - S_{H2}$). In order to check the accuracy of the reactivity measurements, the carbon molar balance was calculated and found to be within < 10% for all reported experiments [Eq. (5)].

$$n_{CH_3OH,in} = n_{CH_3OH,out} + n_{CO} + n_{CO_2} \quad (5)$$

2.4. Analysis of Cu oxidation state

X-ray photoelectron spectroscopy (ESCALAB 250XI, Thermo Scientific, Inc.) was used to determine the Cu oxidation states in the catalysts ex-situ after undergoing POM for various extents of time. After a specified time interval, the reaction was stopped by purging the system with Ar gas flow, and the sample was cooled to room temperature in Ar flow and stored under vacuum for transfer to XPS analysis. A fresh catalyst sample was used for measurement at each time interval. Cu $L_3M_{45}M_{45}$ Auger spectra were obtained for each sample with a monochromated, micro-focused Al Kα X-ray source (spot size = 200 μm; step size = 0.1 eV, pass energy = 50 eV). In order to identify and quantify Cu oxidation states from Cu Auger spectra, reference spectra of each copper oxidation state were collected from pure Cu NPs with similar particle size by the same instrument (Fig. S2). Each reference spectrum has a characteristic peak at an electron kinetic energy of 918.7 eV, 916.8 eV, and 917.6 eV for Cu, Cu_2O, and CuO, respectively. The quantification of Cu oxidation states via Cu Auger lines was implemented following Holse et al. [15]. A linear combination of three reference spectra was fitted to Cu $L_3M_{45}M_{45}$ Auger lines collected via XPS, and the relative amount of each oxidation state was determined from this fit. The errors in the relative ratios were determined at the 99% confidence level, or 3 standard deviations (3σ) of the mean relative ratio values.

2.5. First-principles calculations

First-principles DFT calculations were performed using the Vienna Ab-initio Simulation Package (VASP) [16–19] with the PW91 parameterization of the generalized gradient approximation (GGA) functional [20] and projector augmented wave (PAW) [21,22] pseudopotentials. Atomic structures and charge differences were visualized via the VESTA package [23,24]. The climbing image nudged elastic band ((CI-NEB)) method [25] was applied to calculate POM reaction energy barriers, applying five intermediate images between initial and final stable adsorption states. In order to account for the strong electronic correlation shown to affect the energetics of Cu_2O and related systems, [26,27] the rotationally invariant Dudarev implementation of the

Hubbard *U* model was used to account for electron-electron interaction error in DFT calculations, combining both Coulombic and exchange terms into a single effective *U* parameter (U_{eff}) to account for exchange-correlation errors on Cu 3*d* orbitals[28]. To account for Hubbard U induced changes on Cu-O structures adjacent to reactant species and related energetics [29,30], we found an *a priori* resolved bulk Cu_2O U_{eff} value of 7.45 ± 0.54 eV, which was applied to Cu in surface calculations as 7.5 eV. [31,32] Relative to past research, the measurement uncertainty in this Hubbard U calculation spans the effect magnitude (about 0.3 eV) observed when changing the coordination of oxygen-bonded metal atoms in similar surface systems [33], while also being consistent with previously fitted empirical properties involving Cu-O bulk and surface systems. [34]

Cu_2O surfaces were simulated by slabs including 4 Cu layers. Since the unit cell sizes associated with the (100), (110) and (111) surfaces differed, different periodic surface repetitions were applied to obtain similarly sized surfaces. The bottom two layers of each surface were fixed at their bulk determined positions, while all other atoms were allowed to fully relax during structural optimization. Overall, structural specifications for modeling the surfaces studied in this work were established through past work on related systems [35]. Further information on calculation criteria, content related to the handling of electronic correlation effects, and specifications of the structures modeled in this study can be accessed in the Supporting Information.

3. Results

3.1. Cu/ZnO characterization

30 wt% Cu/ZnO catalysts were synthesized by co-precipitating copper nitrate and zinc nitrate aqueous solution and calcination in air at 400 °C, resulting in the formation of copper oxide and zinc oxide. Subsequent reduction with H_2 under 250 °C for 2 h reduced the CuO phase, yielding the final Cu°/ZnO catalyst [4,5,13]. Characterization of the powdered catalysts by XRD (Fig. 1) confirms that Cu oxide was reduced to metallic Cu while ZnO remained oxidized under these conditions. Based on Scherrer's equation, the crystallite sizes of CuO and ZnO after calcination were calculated to be 4.0 nm and 7.8 nm, respectively. After reduction, Cu and ZnO showed crystallite sizes of 6.7 nm and 10.3 nm, respectively.

SEM measurements (Fig. 2) reveal the morphology of the CuO/ZnO catalyst. EDX measurements show a weight loading of CuO 32.25wt%, close to the initial mass ratio applied during synthesis (Cu:Zn = 3:7). Cu and ZnO NPs are randomly dispersed in the catalyst (see Fig. 3B) and show similar sizes with a fairly narrow size distribution and an average particle size of 7.31 ± 1.49 nm (inset, Fig. 3A), in good agreement with the particle sizes calculated from XRD. HRTEM (Fig. 3B) confirms the random localization and spatial elemental distributions of Cu and ZnO on the nanoscale.

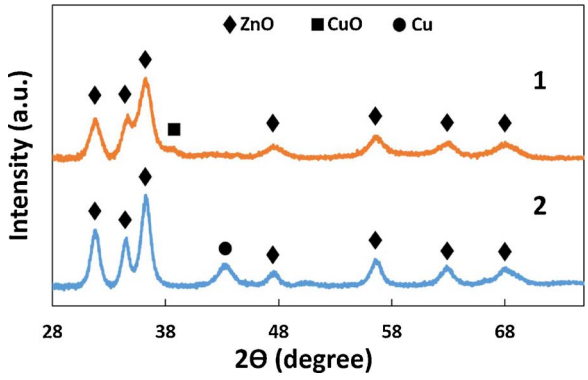

Fig. 1. Powder XRD patterns of as-prepared CuO/ZnO (1) and Cu/ZnO after being reduced in H_2 at 250 °C for 3 h (2).

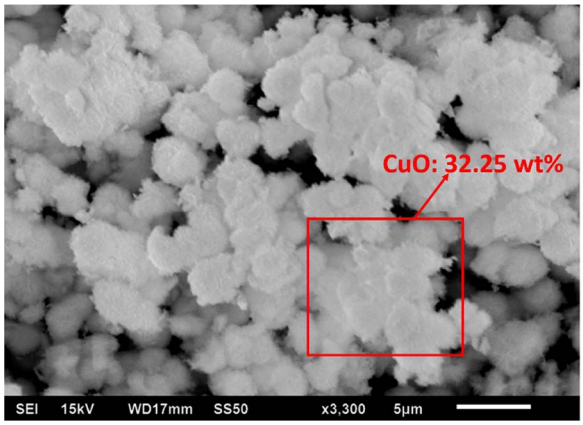

Fig. 2. SEM image of CuO/ZnO as prepared. EDX indicates 32.25 wt% CuO for the area marked by the red box. (For interpretation of the references to colour in this figure legend, the reader is referred to the web version of this article).

3.2. Impact of O_2/MeOH molar feed ratio on POM reactivity

The catalytic performance of the 30 wt% Cu/ZnO during the partial oxidation of methanol (POM) was evaluated in a microreactor setup. Fig. 4 shows measurements of POM reactivity at 250 °C for three different O_2/MeOH molar feed ratios.

The conversion of methanol as a function of time-on-stream is shown in Fig. 4A. At O_2/MeOH = 0.1, methanol conversion increases from 25% to about 40% after 1 h. With increasing O_2/MeOH ratio, methanol conversion increases overall and continues to show this increase with time on stream (from 52%–64% for O_2/MeOH = 0.3, and from 63% to 81% for O_2/MeOH = 0.5 over 1 h time-on-stream). It is reasonable to assume that these gradual increases result from a slow oxidation of the Cu phase in the catalyst, increasing the availability of lattice oxygen for the partial oxidation reaction. Since the relative concentration of O_2 in the feed is below or equal to the O_2/MeOH stoichiometric ratio of 0.5, O_2 is a limiting reactant and O_2 conversion is hence complete at all three feed ratios (not shown here).

Selectivity of the POM reaction is shown in Fig. 4B and C for H_2 and CO_2 formation, respectively. H_2 selectivity (Fig. 4B) starts at 100% and 86% for O_2/MeOH = 0.3 and 0.5 and subsequently drops to 70% and 15%, respectively. For O_2/MeOH = 0.1, the H_2 selectivity is maintained at ~100% for 15 min and then decreased gradually over time. Finally, for the stoichiometric feed (O_2/MeOH = 0.5), H_2 selectivity levels off after ~20 min time on stream at 15% and remains unchanged for the remainder of the reaction time.

Unlike the significant change observed in H_2 selectivity, CO_2 selectivity (Fig. 4C) remains constant over the entire reaction time (~1 h) but drops significantly with decreasing of O_2/MeOH ratio from 88% (O_2/MeOH = 0.5) over ~50% (O_2/MeOH = 0.3), to ~30% (O_2/MeOH = 0.1).

Overall, these results show, unsurprisingly, that both conversion and selectivity in POM strongly depend on oxygen availability, i.e. on the O_2 concentration in the gas phase: Higher O_2 partial pressure leads to higher methanol conversion, lower H_2 selectivity, and higher CO_2 selectivity. This is consistent with prior reports in the literature [4,36] and is an expected result since increasing availability of the oxidant (O_2) as the limiting reactant at these conditions will result in increased conversion and deeper oxidation of the fuel (methanol).

However, the difference in behavior over time between H_2 selectivity and CO_2 selectivity is surprising: If this trend is correlated with a change in catalyst oxidation state, one would assume that the same trend (i.e. increase or decrease in selectivity) would likely be observed for the selectivity along both the C and the H oxidation pathways. Therefore, we investigated the oxidation state of the catalyst at various stages of the reaction next.

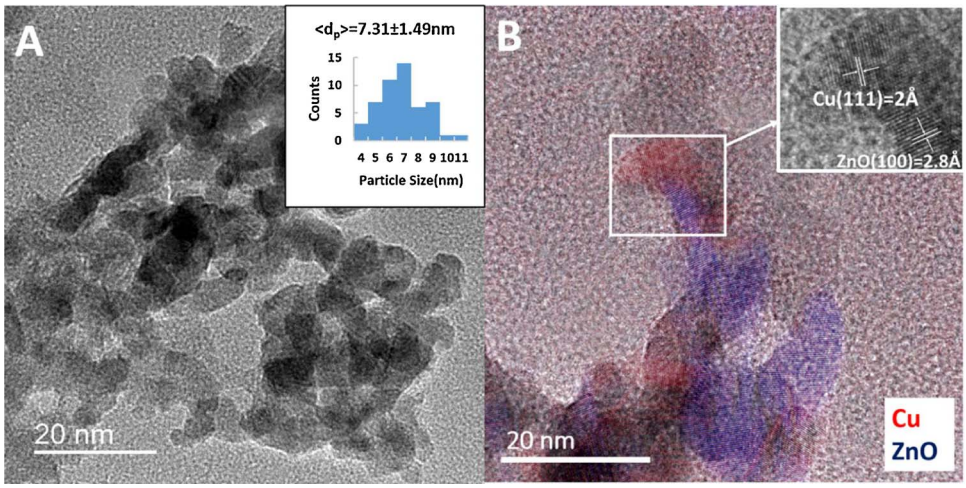

Fig. 3. (A) TEM image of the Cu/ZnO NPs after reduction. Inset: Cu and ZnO NP size distribution. (B) HRTEM image with superimposed (colored) crystal phase domains of Cu and ZnO. Inset: Example of a high magnification image showing Cu° and ZnO lattice spacing. (For interpretation of the references to colour in this figure legend, the reader is referred to the web version of this article).

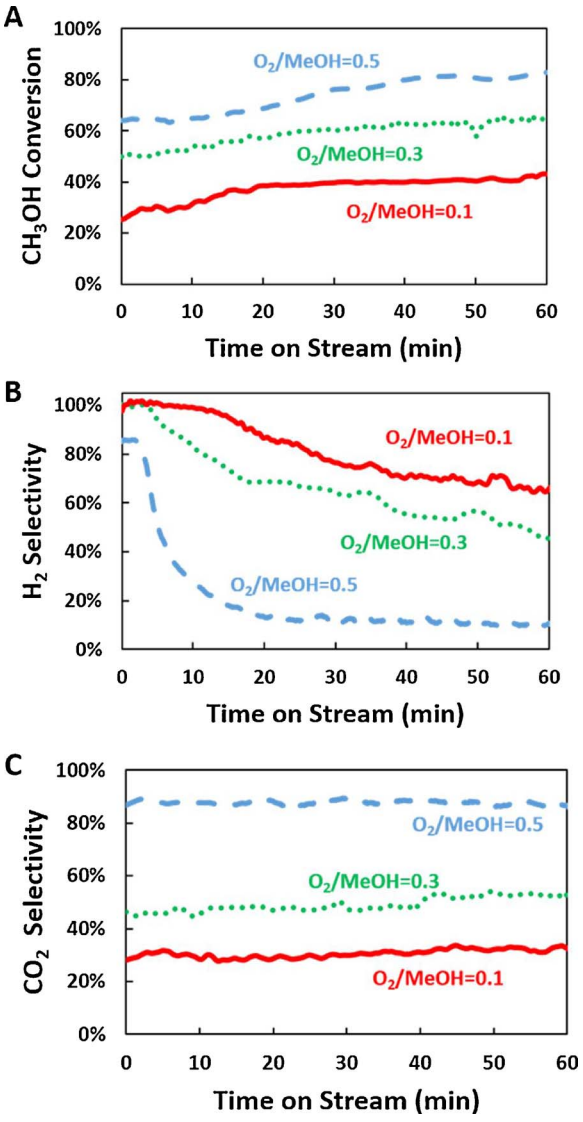

Fig. 4. POM reactivity measurements showing the methanol conversion (A), H_2 selectivity (B), and CO_2 selectivity (C) vs. time-on-stream during POM at 250 °C for three different O_2/MeOH molar ratios (red = 0.1, green = 0.3, and blue = 0.5). MeOH conversion increases and H_2 selectivity decreases with O_2/MeOH molar ratio and time-on-stream. CO_2 selectivity increases with O_2/MeOH molar ratio but remains constant with time-on-stream. (For interpretation of the references to colour in this figure legend, the reader is referred to the web version of this article).

3.3. Change of Cu oxidation state during POM

In order to trace the oxidation state of Cu in the catalyst during the reaction, the samples were quenched via Ar purge and cooled to room temperature, followed by transfer under a vacuum to XPS studies. Previous studies reported that ZnO remains in its oxidized form during POM [9,37–39], which we also confirmed for the present study (Fig. S5). In contrast, Cu is easily oxidized and reduced at POM conditions, and the Cu oxidation states present in the Cu/ZnO-catalysts were hence determined from the positions of the Cu Auger $L_3M_{45}M_{45}$ peaks. Cu° and Cu^{1+} present very similar Cu $2p_{3/2}$ peak positions of ~932.8 eV but show distinct Cu $L_3M_{45}M_{45}$ energies of 918.7 eV and 916.8 eV, respectively, with the Cu^{2+} $L_3M_{45}M_{45}$ peak positioned at 917.6 eV [5,10,14]. Therefore, Cu $L_3M_{45}M_{45}$ Auger spectra were collected to analyze Cu oxidation states.

Fig. 5 shows representative Cu $L_3M_{45}M_{45}$ Auger spectra taken after different times on stream during POM for a feed ratio (O_2/MeOH) of 0.1. The spectra confirm qualitatively that Cu° is being gradually oxidized to Cu_2O throughout the POM reaction. A similar analysis was conducted for samples collected at 0.3 and 0.5 O_2/MeOH feed ratios (see Figs. S3 and S4).

This observation is quantified further in Fig. 6, where the XPS data for the three different feed ratios are summarized by showing the relative percentage of Cu°, Cu^{1+}, and Cu^{2+} vs time-on-stream. For the lowest O_2/MeOH ratio of 0.1 (Fig. 6A), one can see that 5 min after the start of the reaction, the relative Cu° concentration has dropped from 100% to 80% and subsequently decreases further to ~30% at t = 1 h. In parallel, the relative Cu^{1+} concentration increases from 10% to > 60%. The Cu^{2+} concentration remains at ~10% or below for the entire duration of the reaction, indicating that oxidation to Cu^{2+} is hindered by the low oxygen availability.

Fig. 6B and C show the temporal evaluation of Cu for the other two O_2/MeOH ratios studied (0.3 and 0.5, respectively). Changes in Cu oxidation state follow the same trends as those described above for O_2/MeOH = 0.1. However, with increasing O_2 concentration in the gas phase, the oxidation of Cu° proceeds more rapidly and Cu^{1+} quickly becomes the dominant oxidation state in the catalyst. Specifically, for O_2/MeOH = 0.5, the Cu^{1+} concentration rapidly increases from 0% to almost 60% already after 5 min on stream, while at the same time this concentration only increased to ~50% and 10% for O_2/MeOH = 0.3 and 0.1, respectively.

Overall, these results demonstrate that the Cu oxidation state in the Cu/ZnO catalyst is changing dynamically during POM and that this change is strongly influenced by the feed composition. Cu^{2+} remains below 20% at all conditions and shows no significant change over time, indicating that it is not a reaction-relevant species. The dominant Cu

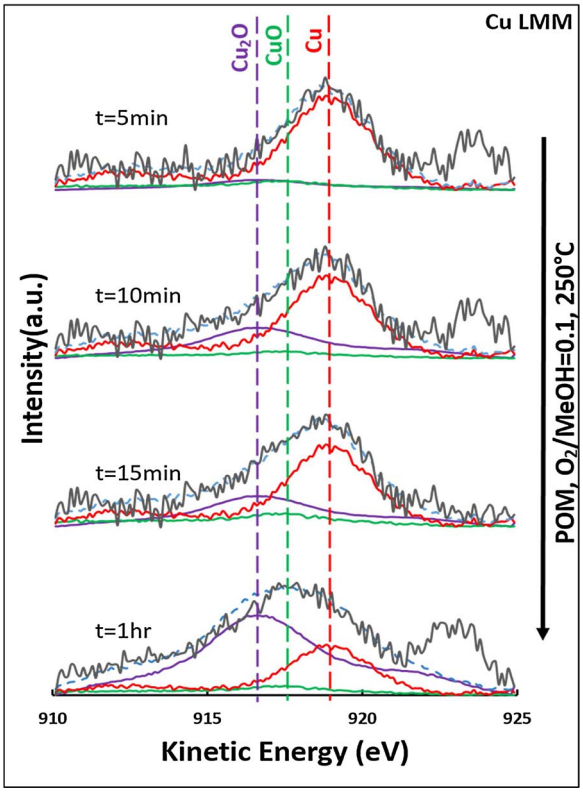

Fig. 5. Changes to the XPS Cu $L_3M_{45}M_{45}$ feature during POM at 250 °C, O_2/MeOH = 0.1. Data points are shown as black lines, while the light blue dashed lines indicate fitted results. The vertical lines indicate peak position for Cu (red), CuO (green), and Cu_2O (purple). The fit in (A) is obtained by fitting a linear combination of three Cu $L_3M_{45}M_{45}$ basis reference spectra (see Fig. S2). (For interpretation of the references to colour in this figure legend, the reader is referred to the web version of this article).

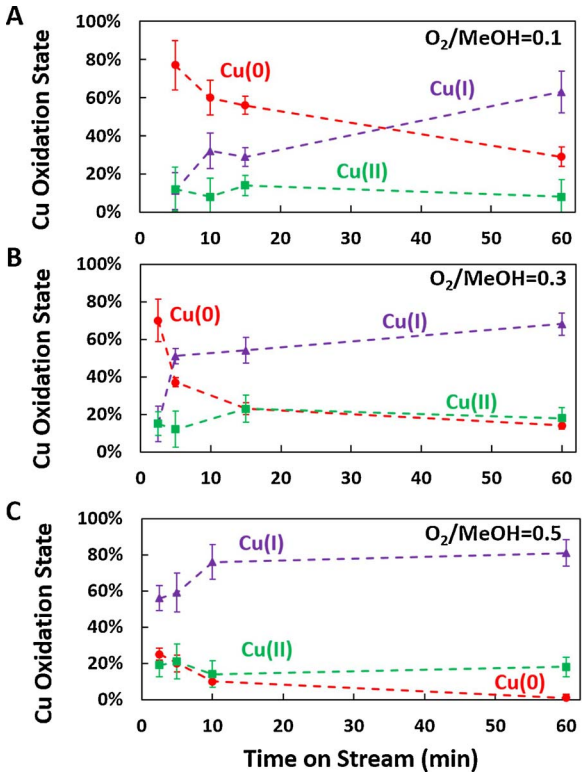

Fig. 6. The relative amount of each Cu oxidation state observed in the catalyst as a function of reaction time at the three molar O_2/MeOH feed ratios of 0.1 (A), 0.3 (B), and 0.5 (C).

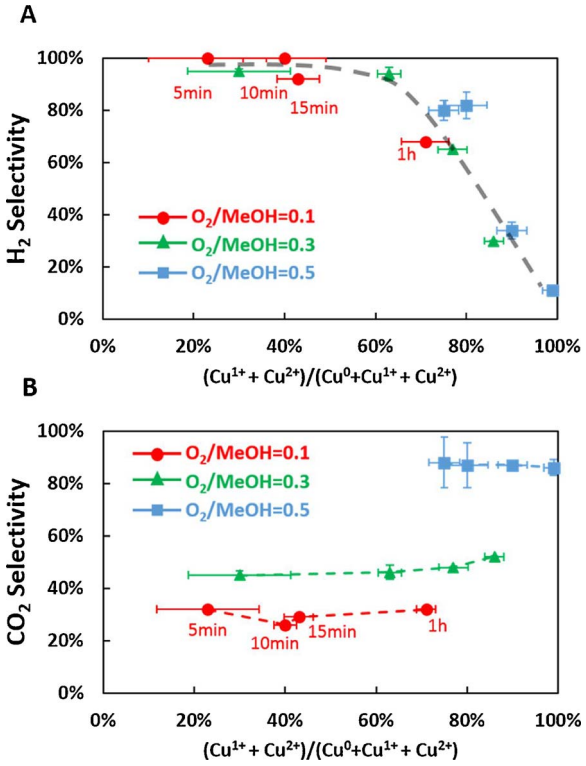

Fig. 7. H_2 selectivity (A) and CO_2 selectivity (B) versus percentage of combined oxidized Cu during the POM reaction at 250 °C and over three different O_2/MeOH molar ratios (red circles = 0.1, green triangles = 0.3, and blue squares = 0.5). (For interpretation of the references to colour in this figure legend, the reader is referred to the web version of this article).

oxidation state over a wide range of reaction conditions is Cu^{1+}, in agreement with previous reports [37].

3.4. Effect of Cu oxidation state on POM selectivity

In order to illustrate correlations between reactivity and Cu oxidation state, Fig. 7 combines the results from the reactivity studies (Fig. 4) and the XPS investigations (Fig. 6). Fig. 7 plots methanol conversion and H_2 and CO_2 selectivities vs. relative amounts of oxidized Cu species (i.e. Cu^{1+} and Cu^{2+}) in the catalyst over time, displaying all three O_2/MeOH feed ratios studied (O_2/MeOH = 0.1, circles; O_2/MeOH = 0.3, triangles; and O_2/MeOH = 0.1, squares).

Remarkably, the H_2 selectivity data gathered at the three different feed ratios collapse onto a single curve (Fig. 7A), i.e. H_2 selectivity appears to *only* depend on the (average) Cu oxidation state in the catalyst: H_2 selectivity is near 100% up to ~50% Cu° content, and then drops rapidly with further increase in the degree of Cu oxidation (Cu^{1+} and Cu^{2+}) in the catalyst. This apparent oxidation of H_2 with lattice O in Cu oxides, reducing Cu oxides while producing H_2O, is in agreement with previous reports [5,10,13,14,37]. The O_2 concentration in the gas phase hence seems to impact H_2 selectivity only indirectly via controlling the oxidation state of Cu.

In contrast to that, Fig. 7B shows that CO_2 selectivity has virtually no correlation with the Cu oxidation state as CO_2 selectivity remains constant over a wide range of Cu° concentrations at any given O_2/MeOH ratio. Instead, CO_2 selectivity depends strongly on the O_2 concentration in the feed gas. This observation contradicts previous work, which suggests, somewhat counter-intuitively, that Cu° favors formation of CO_2 and Cu^{1+} favors CO formation [5]. However, the transient, time-resolved reactivity measurements in the present study (compared to steady-state measurement in the previous work) [5] enable us to capture the temporal dynamics of the reaction kinetics and thus reveal a

rather clear and unambiguous correlation of CO_2 selectivity with gas phase oxygen, rather than lattice oxygen.

Overall, our results thus show that H_2 production is entirely controlled by the Cu oxidation state, while no correlation between CO_2 production and Cu oxidation state is observed and CO_2 production is entirely governed by the oxygen partial pressure in the gas phase. Furthermore, the concentration of Cu^{1+} increases with reaction time, consistently becoming the dominant Cu oxidation state at each feed condition as the reaction approaches steady state. This suggests different reaction pathways of the metallic Cu and Cu_2O surfaces, respectively, observed at the earlier and later stages of the POM reaction, which will be further discussed below.

4. Discussion

4.1. Proposed POM mechanism on Cu and Cu_2O

Overall, our results suggest that the POM reaction mechanism is controlled both by the oxidation state of the catalyst and the prevalence of gas-phase oxygen. It seems hence helpful to break down the mechanistic discussion of the reaction into four cases: POM on metallic (Cu^0) and on oxidized (Cu^{1+}) surfaces, respectively, each in the presence and absence of gas phase oxygen, respectively.

Numerous mechanisms for POM on Cu^0 surfaces have been derived either experimentally or theoretically [6,36,40–42]. As previous studies have mentioned, the overall reaction pathway for POM may be considered as a combination of partial oxidation, steam reforming, methanol decomposition, water-gas shift, and reverse water-gas shift reactions, all of which share the same set of reaction intermediates [36]. In fact, POM on Cu^0 surfaces also shares reaction intermediates with methanol synthesis from H_2 and CO_2 (a slightly modified inverse reaction to POM) such as CH_3O^*, CH_2O^*, and $HCOO^*$ that are well-studied in the literature [29,43,44]. Therefore, the POM reaction mechanism on Cu^0 surfaces is summarized in Fig. 8A: In the presence of gas phase oxygen (Pathway A), the reaction starts with O—H bond activation facilitated by chemisorbed O on the surface. The resulting CH_2O^* is further oxidized by neighboring OH* to form $HCOOH^*$ and then $HCOO^*$. Finally, decomposition of $HCOO^*$ gives CO_2 and H_2 as final products [3,14]. In the absence of O_2 in the feed gas (Pathway B), methanol will follow a decomposition pathway on metallic Cu to generate CO and H_2, i.e., the reverse reaction of methanol synthesis via CO hydrogenation, as shown in Fig. 8B [45]. Both of these mechanisms on a Cu^0 surface have been studied in detail before and are hence supported by multiple studies in the existing literature [5,12,36,37,40,46].

In contrast, very few studies investigated the influence of Cu oxidation state on the POM mechanism [47]. Therefore, we are proposing a mechanism for POM on Cu_2O in order to explain the impact of the Cu oxidation state on POM selectivity observed in our experiments.

Fig. 8C illustrates the proposed POM reaction pathway on Cu_2O in the presence of gas phase oxygen. CH_3OH, CH_3O^* and CH_2O^* bond to Cu_2O surfaces via their O atoms, according to previous studies [34]. The H atom from dissociative methanol adsorption bonds to lattice oxygen and can reduce the oxide surface via water formation [29]. In the presence of gas phase O_2, O vacancies resulting from this desorption can be refilled quickly by chemisorbed O [48]. In contrast with the reaction pathway on Cu^0 (Fig. 8A), in which CH_2O^* is oxidized by adjacent OH* to form $HCOOH^*$, we propose that the corresponding pathway on Cu_2O (Fig. 8C) features further decomposition of CH_2O^* to CHO^* via O—H bond activation [29]. The CHO^* on Cu_2O then gives H to neighboring lattice O, subsequently becoming further oxidized by OH* to $COOH^*$ via a reverse water gas shift reaction step[49]. In this proposed mechanism, further decomposition of $COOH^*$ will then yield CO_2 as the final product [29,49].

In contrast, the POM reaction pathway on Cu_2O in the absence of gas phase oxygen (Fig. 8D) is proposed to proceed via a sequence of CH_3OH dehydrogenation steps, since there is no surface O to facilitate OH* formation. This sequence forms CO as a final product, while the dissociated H* atoms will be oxidized by lattice O and form H_2O as the final product.

4.2. First-principles evaluation of proposed reaction mechanisms

The proposed mechanisms are consistent with the experimental observations summarized in Fig. 7: Regarding the dependence of H_2 selectivity on Cu oxidation state, the proposed mechanisms show a switch from H_2 to H_2O as a predominant final product when moving from metallic Cu to Cu_2O, since lattice O can be accessed by H and removed via water formation. Therefore, H_2 selectivity is controlled by the Cu oxidation state. This observation is further supported by recent literature which indicates that the energy barrier of forming H_2 from associative desorption of two H* (0.29 eV) is much lower than the energy barrier of forming H_2O from H* and OH* (1.39 eV) on Cu(111) surfaces [29,30]. Similar results can also be found on the Cu(110) surface [41]. Thus, H_2 formation would be energetically favored over H_2O on Cu surface ever with O_2 present in the gas phase.

As to CO_2 selectivity, in agreement with our experimental observations, the formation of CO_2 is favored over the formation of CO in the presence of gas phase oxygen (Fig. 8A and C). Switching from Cu (Fig. 8A, B) to Cu_2O (Fig. 8C, D) does not shift the preference of product formation from CO to CO_2, mainly because lattice O does not directly interact with adsorbed CO species.

The methanol synthesis/POM reaction system has been studied previously in much detail for (metallic) Cu surfaces and is well reported in the published literature [29,30,41]. In contrast, the reaction mechanism over Cu_2O has been studied much less and is hence less well understood. The key – and so far unproven – assumption in the proposed mechanism is hence the lack of lattice O interaction in Cu_2O with CO, which results in the preference for CO over CO_2 selectivity that is particularly prevalent in environments featuring a high Cu oxidation state (Cu_2O) and low O_2 partial pressure (Fig. 8D). In order to verify this assumption, DFT calculations were employed to evaluate the formation of CO_2 from surface CO and subsequent desorption of CO_2, as well as the direct desorption of surface CO, on the three low index planes [(100), (110), and (111)] of Cu_2O. The results of these calculations are shown in Fig. 9. Since the facets present on the actual catalytic NPs are unknown, we selected these three low index surfaces, as testing every possible facet is computationally unfeasible and these low index planes are the most stable and hence typically most prevalent surface orientations. The energy barriers for the formation of CO_2 (E_a) and CO desorption (E_d) reactions were compared over the three surfaces, as well as the total energy differences between initial reactants and final products (ΔE). CO_2 is formed by CO bonding with a nearby lattice O atom, which was highlighted in Fig. 9 in light red for clarity. The O-terminated (100) and (111) surfaces are covered with O atoms that have low coordination numbers, which make the O atoms behave like adsorbed O atoms, rather than lattice O. In addition, O-terminated surfaces indicate a high O_2 partial pressure scenario not representative of the previously mentioned environment in which CO desorption is selected over CO_2 formation [48]. Thus, Cu-terminated surfaces were chosen for (100) and (111) surfaces. The Cu-O terminated surface was used for the (110), as this termination contains lattice O in the uppermost layer. These terminations feature lattice O near the surface accessible to adsorbed CO species for CO_2 formation.

The most stable configurations for CO and CO_2 on Cu_2O surfaces were found by testing different orientations and adsorption sites (i.e. horizontal and vertical orientations and bonding via C or O). For the (100) surface, CO and CO_2 are found most stable on the Cu bridge sites. For the (110) and (111) surfaces, CO and CO_2 are found most stable on the Cu top sites. CO_2 was found to be weakly adsorbed on all three surfaces compared to CO. Adsorption configurations and energies can be accessed in the Supporting Information. CO_2 is adsorbed on the surface, with the single lattice O atom removed. CO desorption was

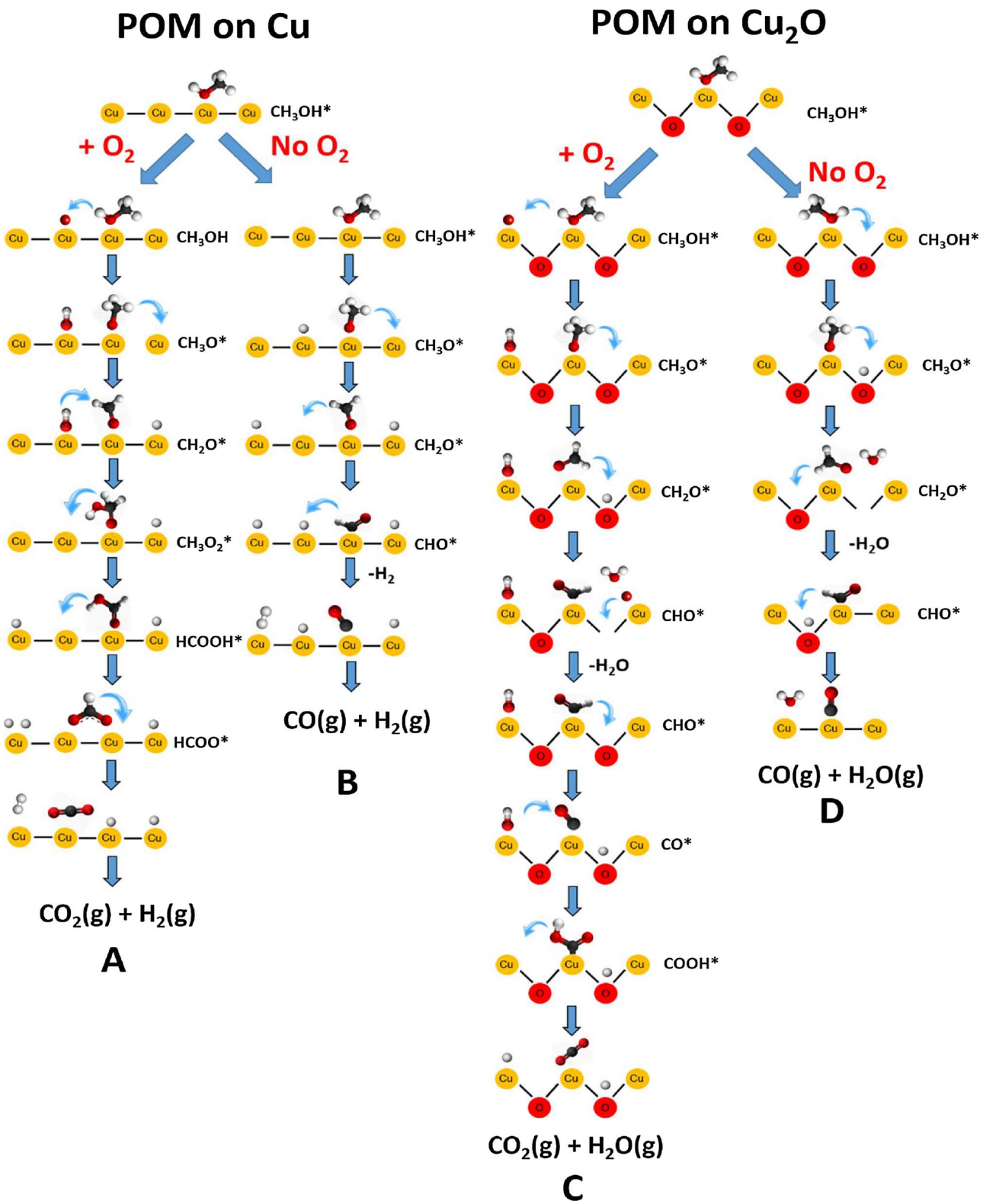

Fig. 8. Proposed schematic reaction pathway of POM on Cu and Cu_2O at different feed conditions, namely: POM (A) and methanol decomposition (in the absence of gas phase O_2; B) on metallic Cu, respectively, and POM in the presence (C) and in absence of gas phase O_2 (D) on Cu_2O. Atoms C (black), H (white), O (red), and Cu (yellow) are colored accordingly. (For interpretation of the references to colour in this figure legend, the reader is referred to the web version of this article).

simulated by placing the CO molecule far above the surface (over 4 Å above the surface).

Fig. 9 summarizes the key results: For the (100) and (110) surfaces, the energy barriers for CO_2 formation (E_a) are higher than the CO desorption energies (E_d), indicating a preference for CO desorption. In contrast, for the (111) surface, the energy barrier for CO_2 formation is lower than the CO desorption energy. Differences between initial and final state energies (ΔE) of adsorbed CO oxidizing to CO_2 are negative for (100) and (110) surfaces (-0.61 and -0.73 eV, respectively), while the ΔE between adsorbed CO and desorbed CO are positive (1.21 and

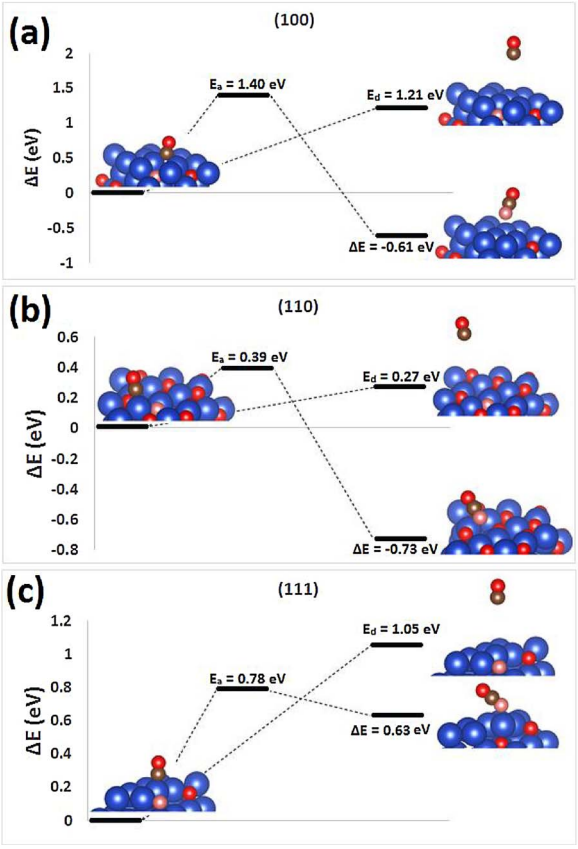

Fig. 9. Energy differences and activation barriers for CO_2 formation and CO desorption on Cu_2O (a) (100), (b) (110), and (c) (111) surfaces. Atoms C (brown), Cu (blue), O (red; marked in light red if the lattice O is used to form CO_2) are colored accordingly. (For interpretation of the references to colour in this figure legend, the reader is referred to the web version of this article).

0.27 eV). However, the ΔE between adsorbed CO and CO_2, and the ΔE between adsorbed vs. desorbed CO for the (111) surface are both positive (0.63 and 1.05 eV, respectively). Since the activation barrier for CO_2 decomposition on (111) is only 0.15 eV, CO desorption may be competitive with CO oxidation. The positive ΔE for CO oxidation on the (111) surface could be explained by the formation of an oxygen vacancy in the second layer. Compared to the (100) and (110) surfaces, the oxygen vacancy formation energy on (111) surface is 1.39 eV and 0.48 eV higher, respectively. This indicates that the oxygen vacancy causes the (111) surface to be more unstable after CO oxidation compared to oxygen vacancies for the (100) and (110) surfaces. Note that the CO desorption barriers (E_d) are the same as ΔE for CO desorption, since CO desorption is a non-activated step.

Our theoretical results for the (100) and (110) surfaces agree with our key experimental observations of unidentifiable catalyst surface facets. Even on oxidized Cu surfaces, adsorbed CO prefers to desorb rather than interact with lattice O atoms to form CO_2 in low O_2 partial pressure environments, hence rendering CO_2 selectivity insensitive to the oxidation state of the catalyst.

5. Conclusion

The present study aimed to elucidate the reaction mechanism of methanol partial oxidation to H_2 and CO_2 on Cu catalysts. A specific focus was the dependence of reaction selectivity on the oxidation state of the catalyst. We found that MeOH conversion and reaction selectivity to H_2 and CO_2 is strongly affected by the O_2/MeOH feed ratio and shows a strong dependence on time-on-stream while approaching steady state. Post-reaction analysis by XPS revealed that during this transient Cu° was gradually oxidized to Cu_2O and that the rate of this oxidation depends on the O_2 partial pressure in the gas phase. Crucially, H_2 selectivity depends strongly on the presence of metallic Cu, i.e. it increases with increasing concentration of Cu°. On the other hand, CO_2 selectivity shows no dependence on Cu oxidation states and instead is controlled by the O_2 concentration in the gas phase. These observations were explained by a lack of interaction between adsorbed CO and lattice oxygen in Cu_2O, i.e. by the fact that CO_2 formation occurred exclusively through interaction with chemisorbed surface oxygen, as confirmed via DFT calculations. In contrast, H_2 can easily access lattice oxygen to form H_2O. It is worth to mention that we are just proposing possible reaction pathways on Cu/Cu_2O that could explain our experimental observation and providing necessary DFT calculation to the unproven assumption. The present study focused entirely the role of Cu oxidation states in partial oxidation of methanol. It is well known that in methanol synthesis the Cu-ZnO interface plays an important role as well. While we verified that ZnO remains oxidized under all conditions of the reported experiments, it hence seems likely that the Cu-ZnO interface also affects reactivity in partial oxidation of methanol. However, this aspect was beyond the scope of the present studies and suggests that combination of in situ environmental TEM studies with reactivity studies as reported here will be helpful to shed further light on structure-activity correlations for Cu-ZnO catalysts in partial oxidation of methanol.

Overall, the study thus not only produced new insights into the POM mechanism on Cu-based catalysts, but along the way also suggests a rational procedure for optimizing catalyst selectivity in POM: A logical conclusion from this study is that maximizing selectivity toward H_2 and CO_2 requires maintaining Cu in a metallic state within the Cu/ZnO catalyst while at the same time maintaining a high oxygen partial pressure. Clearly, these are contradictory demands, as higher oxygen partial pressures will generally result in faster and deeper oxidation of the catalyst. This hence points towards a target for rational design of next-generation POM catalysts: It is well known that alloying metals can strongly affect their resistance to oxidation [50–53]. Hence, identifying components for alloying of Cu-based catalysts which help to suppress or minimize Cu oxidation may be a promising way to optimize Cu-based POM catalysts for future clean energy applications. First-principles calculations could be used further as a guide and screening tool in such an undertaking.

Acknowledgements

Financial support for this research provided via the National Science Foundation (NSF) under NSF Collaborative Research Award grant CBET 1264637 and 1264940 is gratefully acknowledged. Catalyst characterization was performed at the PINSE Nanoscale Fabrication and Characterization Facility (NFCF) at the University of Pittsburgh, and XPS data were collected at the Materials Characterization Laboratory (MCL) in the Department of Chemistry at the University of Pittsburgh. Theoretical calculations were performed from computing time provided by the Extreme Science and Engineering Discovery Environment (XSEDE) through allocation TG-DMR110009, which is supported by the National Science Foundation grant number ACI-1548562, and by the Center for Functional Nanomaterials, which is a U.S. DOE Office of Science User Facility, at Brookhaven National Laboratory under Contract No. DE-SC0012704.

Appendix A. Supplementary data

Supplementary data associated with this article can be found, in the online version, at https://doi.org/10.1016/j.apcata.2018.02.028.

References

[1] X. Cheng, Z. Shi, N. Glass, L. Zhang, J. Zhang, D. Song, Z.-S. Liu, H. Wang, J. Shen,

J. Power Sources 165 (2007) 739–756.
[2] B.C. Steele, A. Heinzel, Nature 414 (2001) 345–352.
[3] S.H. Oh, R.M. Sinkevitch, J. Catal. 142 (1993) 254–262.
[4] T.-j. Huang, S.-W. Wang, Appl. Catal. 24 (1986) 287–297.
[5] L. Alejo, R. Lago, M.A. Peña, J.L.G. Fierro, Appl. Catal. A Gen. 162 (1997) 281–297.
[6] R.M. Navarro, M.A. Pena, J.L.G. Fierro, J. Catal. 212 (2002) 112–118.
[7] T.-J. Huang, S.-L. Chren, Appl. Catal. 40 (1988) 43–52.
[8] G.C. Chinchen, K.C. Waugh, D.A. Whan, Appl. Catal. 25 (1986) 101–107.
[9] R.M. Navarro, M.A. Pena, C. Merino, J.L.G. Fierro, Top. Catal. 30-1 (2004) 481–486.
[10] I. Eswaramoorthi, V. Sundaramurthy, A. Dalai, Appl. Catal. A Gen. 313 (2006) 22–34.
[11] Y.-C. Lin, K.L. Hohn, S.M. Stagg-Williams, Appl. Catal. A Gen. 327 (2007) 164–172.
[12] Y.-C. Lin, L.T. Fan, S. Shafie, K.L. Hohn, B. Bertók, F. Friedler, Ind. Eng. Chem. Res. 47 (2008) 2523–2527.
[13] J. Agrell, H. Birgersson, M. Boutonnet, I. Melian-Cabrera, R.M. Navarro, J.L.G. Fierro, J. Catal. 219 (2003) 389–403.
[14] S.R. González Carrazán, R. Wojcieszak, R.M. Blanco, C. Mateos-Pedrero, P. Ruiz, Appl. Catal. B Environ. 168–169 (2015) 14–24.
[15] C. Holse, C.F. Elkjær, A. Nierhoff, J. Sehested, I. Chorkendorff, S. Helveg, J.H. Nielsen, J. Phys. Chem. C 119 (5) (2015) 2804–2812 150122080137001.
[16] G. Kresse, J. Furthmuller, Phys. Rev. B Condens. Matter 54 (1996) 11169–11186.
[17] G. Kresse, J. Furthmüller, Comp. Mater. Sci. 6 (1996) 15–50.
[18] G. Kresse, J. Hafner, Phys. Rev. B Condens. Matter 47 (1993) 558–561.
[19] G. Kresse, J. Hafner, Phys. Rev. B Condens. Matter 49 (1994) 14251–14269.
[20] J.P. Perdew, J.A. Chevary, S.H. Vosko, K.A. Jackson, M.R. Pederson, D.J. Singh, C. Fiolhais, Phys. Rev. B Condens. Matter 46 (1992) 6671–6687.
[21] P.E. Blochl, Phys. Rev. B Condens. Matter 50 (1994) 17953–17979.
[22] G. Kresse, D. Joubert, Phys. Rev. B 59 (1999) 1758–1775.
[23] K. Momma, F. Izumi, J. Appl. Crystallogr. 41 (2008) 653–658.
[24] K. Momma, F. Izumi, J. Appl. Cryst. 44 (2011) 1272–1276.
[25] G. Henkelman, B.P. Uberuaga, H. Jónsson, J. Chem. Phys. 113 (2000) 9901–9904.
[26] Y. Maimaiti, M. Nolan, S.D. Elliott, Phys. Chem. Chem. Phys. 16 (2014) 3036–3046.
[27] L. Wang, T. Maxisch, G. Ceder, Phys. Rev. B 73 (2006) 195107.
[28] S.L. Dudarev, G.A. Botton, S.Y. Savrasov, C.J. Humphreys, A.P. Sutton, Phys. Rev. B 57 (1998) 1505–1509.
[29] L.C. Grabow, M. Mavrikakis, ACS Catal. 1 (2011) 365–384.
[30] A.J. Johansson, T. Brinck, Mechanisms and Energetics of Surface Reactions at the Copper-Water Interface, TR-12-07 Swedish Nuclear Fuel Management Co, Stockholm, Sweden, 2012 Search PubMed, 2012.
[31] M. Cococcioni, S. de Gironcoli, Phys. Rev. B 71 (2005) 035105.
[32] M.T. Curnan, J.R. Kitchin, J. Phys. Chem. C 119 (2015) 21060–21071.
[33] U. Aschauer, J. Chen, A. Selloni, Phys. Chem. Chem. Phys. 12 (2010) 12956–12960.
[34] J. Li, G. Zhou, Surf. Sci. 646 (2016) 288–297.
[35] A.A. Padama, H. Kishi, R.L. Arevalo, J.L. Moreno, H. Kasai, M. Taniguchi, M. Uenishi, H. Tanaka, Y. Nishihata, J. Phys. Condens. Matter 24 (2012) 175005.
[36] J. Agrell, H. Birgersson, M. Boutonnet, J. Power Sources 106 (2002) 249–257.
[37] F. Raimondi, K. Geissler, J. Wambach, A. Wokaun, Appl. Surf. Sci. 189 (2002) 59–71.
[38] J. Agrell, M. Boutonnet, J.L.G. Fierro, Appl. Catal. A Gen. 253 (2003) 213–223.
[39] C.-L. Li, Y.-C. Lin, Catal. Lett. 140 (2010) 69–76.
[40] S. Sakong, A. Gros, J. Catal. 231 (2005) 420–429.
[41] S. Sakong, A. Gross, J Phys Chem A 111 (2007) 8814–8822.
[42] S. Sun, Y. Wang, Q. Yang, Appl. Surf. Sci. 313 (2014) 777–783.
[43] M. Behrens, F. Studt, I. Kasatkin, S. Kuhl, M. Havecker, F. Abild-Pedersen, S. Zander, F. Girgsdies, P. Kurr, B.L. Kniep, M. Tovar, R.W. Fischer, J.K. Norskov, R. Schlogl, Science 336 (2012) 893–897.
[44] F. Studt, M. Behrens, E.L. Kunkes, N. Thomas, S. Zander, A. Tarasov, J. Schumann, E. Frei, J.B. Varley, F. Abild-Pedersen, J.K. Nørskov, R. Schlögl, ChemCatChem 7 (2015) 1105–1111.
[45] J. Greeley, M. Mavrikakis, J. Catal. 208 (2002) 291–300.
[46] S. Rabe, F. Vogel, Appl. Catal. B Environ. 84 (2008) 827–834.
[47] K.-Y. Lee, C.-C. Shen, Y.-J. Huang, Ind. Eng. Chem. Res. 53 (2014) 12622–12630.
[48] D. Le, S. Stolbov, T.S. Rahman, Surf. Sci. 603 (2009) 1637–1645.
[49] B.-Z. Sun, W.-K. Chen, Y.-J. Xu, J. Chem. Phys. 133 (2010) 154502.
[50] S. Chen, L. Brown, M. Levendorf, W. Cai, S.-Y. Ju, J. Edgeworth, X. Li, C.W. Magnuson, A. Velamakanni, R.D. Piner, J. Kang, J. Park, R.S. Ruoff, ACS Nano 5 (2011) 1321–1327.
[51] B.A. Pint, J.R. DiStefano, I.G. Wright, Mater. Sci. Eng. A 415 (2006) 255–263.
[52] R. Prescott, M.J. Graham, Oxid. Met. 38 (1992) 233–254.
[53] J. Li, J.W. Mayer, E.G. Colgan, J. Appl. Phys. 70 (1991) 2820–2827.